Disentangling effects of potential shape in the fission rate of heated nuclei

I. I. Gontchar, M. V. Chushnyakova, N. E. Aktaev, A. L. Litnevsky, and E. G. Pavlova
Physics and Chemistry Department, Omsk State Transport University, Omsk, Russia
(Received 25 June 2010; revised manuscript received 29 October 2010; published 21 December 2010)

We have compared the results of dynamical modeling of the fission process with predictions of the Kramers formulas. For the case of large dissipation, there are two of them: the integral rate R_I and its approximation R_O. As the ratio of the fission barrier height B_f to the temperature T reaches 4, any analytical rate is expected to agree with the dynamical quasistationary rate R_D within 2%. The latter has been obtained using numerical modeling with six different potentials. It has been found that the difference between R_O and R_D sometimes exceeds 20%. The features of the potentials used that are responsible for this disagreement are identified and studied. It is demonstrated that it is R_I, not R_O, that meets this expectation regardless of the potential used.

DOI: 10.1103/PhysRevC.82.064606 PACS number(s): 24.75.+i, 05.60.−k, 24.10.Pa, 24.60.Dr

I. INTRODUCTION

The statistical model of the fission process was first introduced by Bohr and Wheeler in Ref. [1]. Soon afterward, Kramers derived several formulas for the fission rate, which included the strength of dissipation corresponding to the nuclear collective motion [2]. One of the formulas and its modifications, sometimes incorporating the Bohr-Wheeler formula, are widely used in modern dissipative statistical models of fission accompanied by light particle emission [3–8]. An alternative way of modeling the process relies on solving numerically the stochastic differential equations [9,10]. These equations allow us to obtain the quasistationary fission rate R_D. Both the Kramers and the dynamical approaches are based on the picture of Brownian motion. The latter method is more accurate but very computer-time-consuming. That is why the combined dynamical-statistical models have been developed [9,10] and are being used widely at present [11–20]. In these models, after a certain delay time, the dynamical modeling is matched to the statistical description. In the latter, a Kramers fission rate is used, implying that the rate agrees approximately with R_D.

The difference between the Kramers fission rates and R_D was shown to reach approximately 20% [21–23]. Let us note that this level of disagreement persists if the peculiarities of the nuclear fission problem related to the microcanonical character of the ensemble are accounted for. Otherwise, the disagreement reaches an order of magnitude (see, e.g., Fig. 7(a) of Ref. [21]).

The discrepancy of 20% was acceptable 20 years ago. Nowadays, there are at least three circumstances that require a more accurate analytical description of the fission rate. First, it was shown [24] that the quantum correction to the Kramers formula was of the order of 10%. Second, the contribution of the memory (non-Markovian) effects may be comparable with the first one [25,26]. The third effect is the multidimensionality of the fission process (see Ref. [27] for details).

The fission rate is crucial for calculating the values of physical observables. For example, if neutron emission is the only channel competing with fission, the first-chance fission probability P_f can be estimated within the framework of the statistical approach: $P_f = (1 + R_n R_{\rm fis}^{-1})^{-1}$. Here R_n and $R_{\rm fis}$ denote the neutron emission and fission rates, respectively. It is easy to see that the 20% relative error in $R_{\rm fis}$ results in the 20% and 10% relative errors in P_f provided $R_n \gg R_{\rm fis}$ and $R_n = R_{\rm fis}$, respectively. This should be compared with the 5%–10% accuracy reached in the modern measurements of fission probabilities or fission cross sections. Here, we no longer concentrate on the physical observables along the lines of Refs. [27–29].

Many aspects of the problem may be responsible for the significant difference between the Kramers rates and R_D, for example, the deformation dependence of the friction (inertia) tensor and of the single-particle level density parameter a, the approximations made in the derivation of the Kramers formulas, and the nonharmonic character of the collective potential. The aims of the present study are as follows: (i) to disentangle the effects of the potential shape in the accuracy of the Kramers formulas, and (ii) to find the conditions under which the discrepancy between R_D and an analytical fission rate is reduced to about 2%. This value is comparable with the statistical errors of R_D achievable during a reasonable amount of computer modeling.

In order to reduce the uncertainties related to all other parameters but the potential shape, the one-dimensional overdamped motion of a Brownian particle representing the fission process is considered. Moreover, the friction and inertia parameters as well as the level density parameter are assumed to be deformation-independent. These are serious restrictions, which, however, are still being used in modern studies [23], [28–30]. In the future, based on the understanding obtained, we plan to consider more realistic situations.

II. DYNAMICAL MODELING

We restrict ourselves to the symmetric fission at zero angular momentum. The shape of the nucleus is characterized by the collective coordinate q, which is equal to half the distance between mass centers of the nascent fragments over the radius of the spherical nucleus. The corresponding conjugate momentum is denoted by p. Initially all the nuclei are assumed to be concentrated at $q_{qs} = 0.375$ at $p = 0$, and the saddle and scission points are located at $q_{sd} = 1.2$ and $q_{sc} = 3.0$, respectively. We deliberately position the

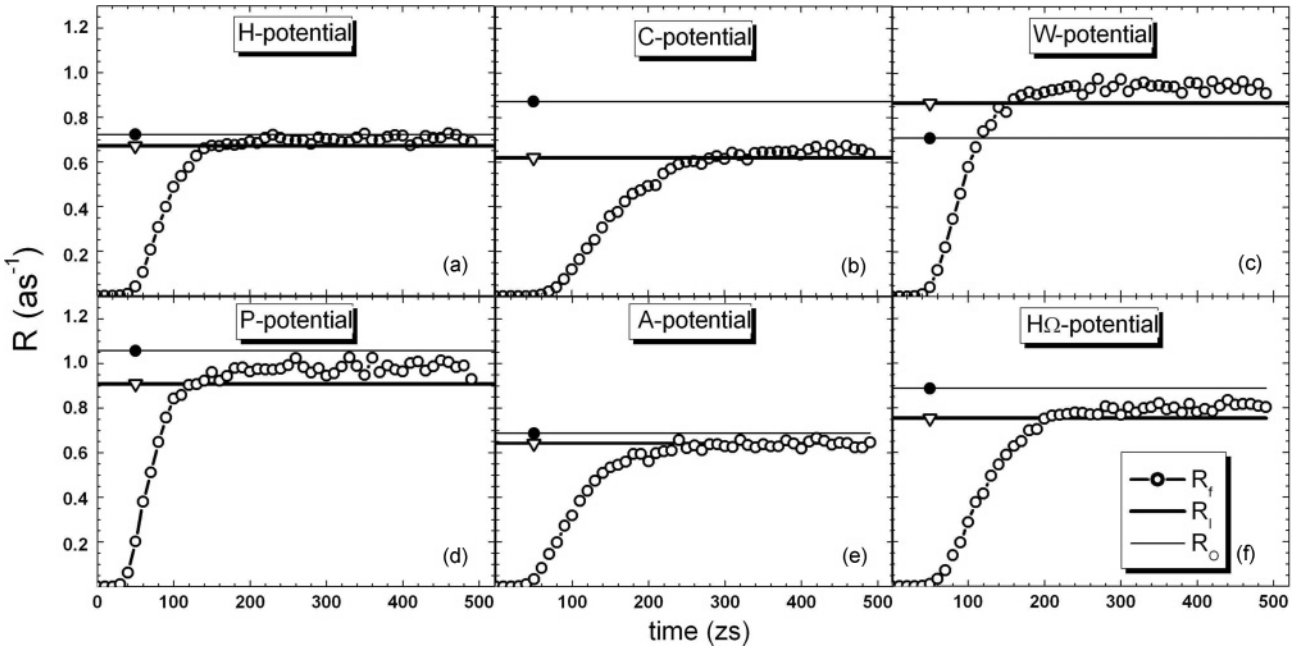

FIG. 1. Fission rates obtained on the basis of dynamical modeling (R_f, lines with open circles) using Eq. (1) with different types of potential (for details, see Sec. IV). One sees the typical behavior of the fission rates reaching their quasistationary values after the relaxation stage. In each panel, the integral Kramers rate R_I [Eq. (3)] is shown by the thick horizontal line with an open triangle, whereas the R_O [Eq. (4)] is displayed by the thin horizontal line with a full circle. In panel (e), R_{O4} [Eq. (13)] instead of R_O is presented. $E_{\rm tot} = 150$ MeV, $B_f/T = 1.95$.

quasistationary, saddle, and scission points far from each other to eliminate the possible influence of the distance between them on our results.

Within our approximations, the nuclear collective motion is modeled using the Euler scheme for the stochastic (Langevin) equation [9,23]

$$q_{n+1} = q_n - \frac{\tau}{\eta}\left(\frac{dU}{dq}\right)_n + b_n\sqrt{\frac{T\tau}{\eta}}. \qquad (1)$$

Here the friction parameter η is related to the damping coefficient β and to the inertia parameter m, $\eta = \beta m$; τ is the time step of dynamical modeling and b_n is a Gaussian random number with a variance of 2. The temperature T is calculated using the Fermi-gas relation, $T = \sqrt{E_{\rm tot}/a}$, and is supposed to be deformation-independent. Earlier (see [31] and references therein), the deformation dependence of η, m, a, and T was accounted for, but it did not allow us to disentangle the influence of the potential shape on the difference between the Kramers rates and R_D. Since η and τ enter into Eq. (1) only as the ratio η/τ, it is sufficient to perform the modeling for one value of the damping coefficient, and $\beta = 10$ zs^{-1} has been chosen. The height of the fission barrier for all calculations of this paper was $B_f = 5.35$ MeV.

Within the framework of the Langevin formalism, the time-dependent fission rate R_f can be calculated by counting the number of trajectories N_f that reach the scission point before the time moment t,

$$R_f(t) = \frac{1}{N_{\rm tot} - N_f(t)}\frac{dN_f(t)}{dt}, \qquad (2)$$

where $N_{\rm tot}$ is the total number of trajectories modeled.

Typical fission rates are shown in Fig. 1 for the six different potentials that are discussed in Sec. IV. The excitation energy is $E_{\rm tot} = 150$ MeV in these calculations. After a transient stage, each $R_f(t)$ reaches its quasistationary value R_D. The time step of modeling $\tau = 0.05$ zs is typically used. In every case, from from 10^5 up to 3×10^5 fissioned trajectories are obtained.

R_D is calculated by averaging R_f over the last 20–30 bins. If the interval of averaging is chosen correctly, R_D does not depend on how many bins are accounted for; it changes within the statistical error. One can see that in the case of the H potential [Fig. 1(a)], the interval between 200 and 500 zs can be taken for this procedure. The same time interval is suitable for the cases of the W, P, and A potentials [Figs. 1(c)–1(e)]. In the case of the C potential [Fig. 1(b)], such an interval results in the wrong value of R_D since R_f reaches its quasistationary value significantly later. R_D is the most important characteristic of the fission process. This is the very value with which we compare the analytical rates in the rest of the paper.

III. ANALYTICAL FORMULAS FOR THE QUASISTATIONARY FISSION RATES AND REPRESENTATION OF THE RESULTS

The Kramers formulas, the accuracy of which we are studying by means of comparison with the dynamical modeling, read

$$R_I = \frac{T}{\eta}\left[\int_{-\infty}^{q_{sd}} \exp\left(-\frac{U(y)}{T}\right)dy \int_{q_{qs}}^{q_{sc}} \exp\left(\frac{U(x)}{T}\right)dx\right]^{-1}, \qquad (3)$$

$$R_O = \frac{\omega_{qs}\omega_{sd}}{2\pi\beta}\exp\left(-\frac{B_f}{T}\right). \quad (4)$$

Here, B_f stands for the fission barrier height, and $\omega_{qs} = \sqrt{C_{qs}/m}$ and $\omega_{sd} = \sqrt{C_{sd}/m}$ are the absolute values of the angular frequencies of the collective motion around the maximum (the saddle point) and the minimum (the quasistationary point) of the potential energy. Equation (3) is supposed to be valid if (i) the fission barrier is high enough compared to the temperature and (ii) β is large enough, that is, $\beta \gg \max(\omega_{qs}, \omega_{sd})$. Equation (4) results from Eq. (3) after extending the limits of integration q_{sd}, q_{sc} to plus infinity, q_{qs} to minus infinity, and expanding the potential energy in the integrands up to the quadratic terms in $y - q_{qs}$ and $x - q_{sd}$. Thus Eq. (4) is valid under the following additional requirements: (iii) The scission point is far enough from the saddle point (this makes it possible to substitute the q_{sc} by plus infinity) and (iv) the potential $U(q)$ is represented near its extremes by two quadratic parabolas with stiffnesses C_{qs} and C_{sd}.

The most familiar Kramers rate widely quoted by the nuclear fission community (see, e.g., [3,7,8,10]) reads

$$R_K = \frac{\omega_{qs}}{2\pi\omega_{sd}}\left(\sqrt{\omega_{sd}^2 + \frac{\beta^2}{4}} - \frac{\beta}{2}\right)\exp\left(-\frac{B_f}{T}\right). \quad (5)$$

We do not use Eq. (5) in this paper and thus we do not discuss the limits of its applicability. Note, however, that Eq. (4) results from Eq. (5) if (ii) holds.

In the original Kramers paper [2], Eq. (3) was not written explicitly; it was implied. This is probably why R_I, to the best of our knowledge, was not used earlier in the literature to model the fission process. Equation (3) resembles the formula for the inverse mean first passage time, R_{MFPT}, which is discussed in detail in Refs. [9,21,28]. However, R_{MFPT} contains double integration whereas R_I is a product of two decoupled integrals. That is why we discuss here only R_I, but not R_{MFPT}. Note that in the literature, most often Eqs. (5) or (4) are used and are called Kramers formulas.

Of the two Kramers fission rates, R_I and R_O, the former is expected to agree better with R_D. We have calculated the three fission rates at values of excitation energy ranging from 9 up to 270 MeV. The rates versus E_{tot} are shown in Fig. 2. They cover three orders of magnitude and are hardly distinguishable.

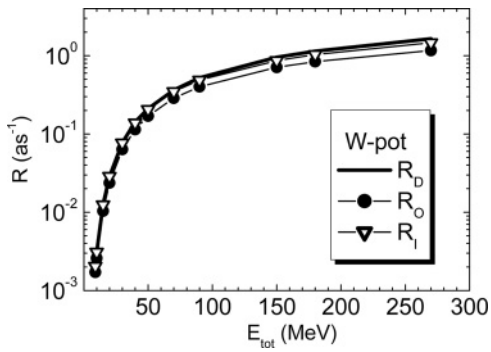

FIG. 2. The fission rates vs excitation energy. The W potential is used (see Sec. IV C for details). The thick solid line corresponds to R_D, full circles indicate R_O, and R_I is shown by open triangles.

Therefore, it is convenient to characterize the deviation of a fission rate R_i from another rate R_j (both calculated with the same potential) by means of the fractional difference

$$\xi_{ij} = \frac{R_i - R_j}{R_j}. \quad (6)$$

These are the ξ_{ij} values that are shown in the following figures. However, the discussion is presented in terms of the rates themselves. For example, $\xi_{OD} = 5\%$ means that the Kramers rate of Eq. (4) exceeds the dynamical quasistationary fission rate by 5%.

IV. THE NUMERICAL FISSION RATES VERSUS THE ANALYTICAL RATES

A. The two-quadratic-parabolas potential with equal stiffnesses (H potential)

This potential is shown in Fig. 3(a) by a thick line with triangles and is referred to later as the H (harmonic) potential. It has been used in many articles (see, e.g., Refs. [25,28,32–35]). The H potential reads

$$U_H(q) = \begin{cases} \dfrac{C_{qs}}{2}(q - q_{qs})^2, & q < q_m, \\ -\dfrac{C_{sd}}{2}(q - q_{sd})^2 + B_f, & q > q_m. \end{cases} \quad (7)$$

Here C_{qs} and C_{sd} are the stiffnesses of the potential near the quasistationary and saddle points, respectively, and q_m

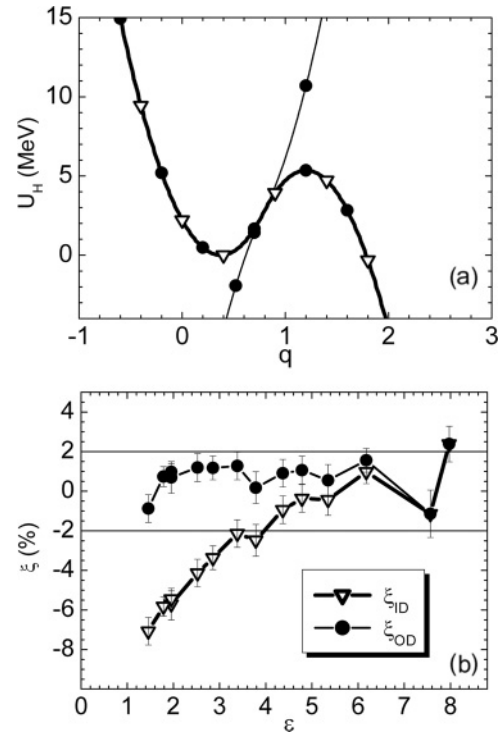

FIG. 3. (a) The H potential (thick line with triangles) and the quadratic parabolas approximating it near the extreme points (thin lines with circles) vs q. (b) The fractional differences ξ_{ID} (open triangles) and ξ_{OD} (full circles) vs $\varepsilon = B_f/T$. The 2% interval near zero is shown by thin horizontal lines.

is the matching point. The H potential stretches into the region of negative-q values that has no physical meaning for the fission process. However, this potential corresponds best to the assumptions under which the Kramers formula (4) was derived. In this subsection, $C_{qs} = C_{sd} = 31.44$ MeV and consequently $\omega_{qs} = \omega_{sd}$; later the case $\omega_{qs} \neq \omega_{sd}$ is studied (see Sec. IV F). Along with the H potential, in Fig. 3(a) the quadratic parabolas from which it is constructed are displayed by thin lines with full circles.

R_I and R_O are expected to agree with the "true" fission rate if $\varepsilon = B_f T^{-1}$ becomes large enough. In Ref. [35] it was shown that R_K of Eq. (5) agreed well with R_D even in the case $\varepsilon = 1$. However, no quantitative analysis was performed in that work. Therefore, we present in Fig. 3(b) the fractional differences ξ_{ID} (triangles) and ξ_{OD} (circles) versus the parameter ε. Since R_O has been derived from the integral Kramers rate R_I, the latter is supposed to agree better with R_D. However, the opposite is seen in Fig. 3(b). This seems to be due to occasional compensation for the inaccuracies made in the derivation of Eq. (4) from Eq. (3). The mutual layout of ξ_{ID} and ξ_{OD} can be explained as follows.

As already mentioned, Eq. (4) results from Eq. (3) if one makes an expansion of the potential energy in the exponents up to quadratic terms in $(y - q_{qs})$ (the left integral) and in $(q_{sd} - x)$ (the right integral). In addition, all the upper limits of integration are changed to plus infinity, whereas minus infinity is used as the lower limits:

$$R_O = \frac{T}{\eta}\left[\int_{-\infty}^{+\infty} \exp\left(-\frac{C_{qs}y^2}{2T}\right) dy \times \int_{-\infty}^{+\infty} \exp\left(\frac{2B_f - C_{sd}x^2}{2T}\right) dx\right]^{-1}. \quad (8)$$

One can think that the expansion does not change anything since the potential is made of the two quadratic parabolas. This would be the case if the integration were performed near the parabolas' extremes. However, in both integrals the limits of integration enter the neighboring parabola. Thus both the expansion of $U(q)$ and the extension of the integral limits are significant. Figure 4 illustrates the influence of these two factors. Here the integrands of Eqs. (3) and (8) are displayed as functions of the integration variable. Shown in panels (a) and (b) are the integrands of the left and right integrals, respectively. The thick lines with open triangles correspond to Eq. (3), whereas the thin lines with full circles are for Eq. (8). In each panel of Fig. 4 near the limits of integration in Eq. (3), its integrand is orders of magnitude larger than the one in Eq. (8). The extension of the limits of integration does not compensate for this effect. The larger integrands result in $R_I < R_O$, which is seen in Fig. 3.

To conclude this subsection, let us note that the fractional difference ξ_{ID} enters the region ± 2 % at the value of ε of about $3.5 - 4.0$ [$\exp(-4) = 0.018$].

B. The cosine potential (C potential)

Of course the shapes of the well and the barrier are not necessarily parabolic. Therefore, we have made calculations

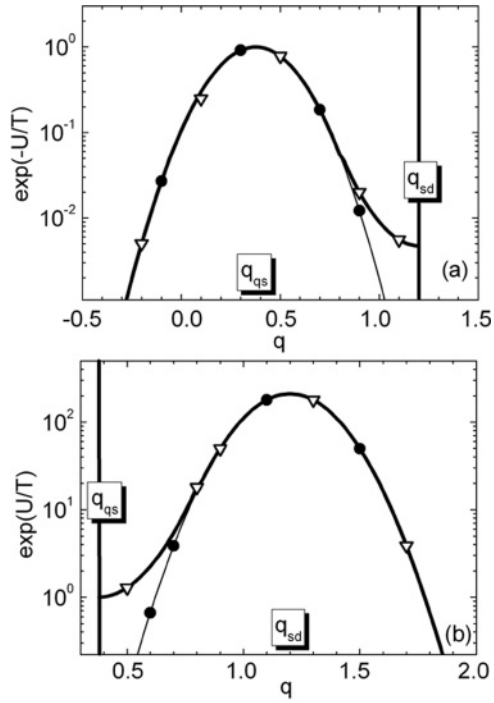

FIG. 4. (a) The integrands of the left integrals used to calculate R_O [Eq. (8), thin line with full circles] and R_I [Eq. (3), thick line with open triangles] are shown as functions of q. The vertical line indicates the finite limit of integration in R_I (the saddle-point coordinate). (b) The curves are the same as in the upper panel but for the right integrals. The vertical line indicates the interior limit of the right integral in Eq. (3) (the quasistationary-state coordinate).

using the cosine potential (C potential) of Ref. [36],

$$U_C(q) = \begin{cases} \frac{B_f}{2}\left(1 - \frac{\pi}{2} - \alpha\right) & \text{if } \alpha < -\frac{\pi}{2}, \\ \frac{B_f}{2}(1 - \cos\alpha) & \text{if } -\frac{\pi}{2} \leqslant \alpha < \frac{3\pi}{2}, \\ \frac{B_f}{2}\left(1 - \alpha + \frac{3\pi}{2}\right) & \text{if } \alpha \geqslant \frac{3\pi}{2}. \end{cases} \quad (9)$$

Here, $\alpha = \pi(q - q_{qs})(q_{sd} - q_{qs})^{-1}$, and the frequencies entering Eq. (4) are fully defined by B_f and $q_{sd} - q_{qs}$. The C potential and the resulting ξ_{OD} and ξ_{ID} are shown in Fig. 5, which is designed exactly like Fig. 3. The value of ξ_{OD} is far from zero, confirming that in the case of the H potential the acceptable agreement between R_O and R_D is purely accidental.

Let us now discuss the difference between R_O and R_I. Equation (4) accounts for only the two quadratic parabolas approximating the C potential near its extremes. The quadratic parabolas have stiffnesses 38.79 MeV and they are shown in Fig. 5(a) by thin lines with circles. The upright parabola clearly contains fewer collective states than the quasistationary well of the C potential itself. This results in $R_O > R_I$. The inverted parabola presents the barrier, which is obviously thinner than that of the C potential. This again enhances R_O in comparison with R_I. Another way to explain the relation between these rates is similar to the discussion concerning Fig. 4.

Comparing Fig. 3(b) and 5(b), we are forced to conclude that Eq. (4) should be used with care. Moreover, only at ε

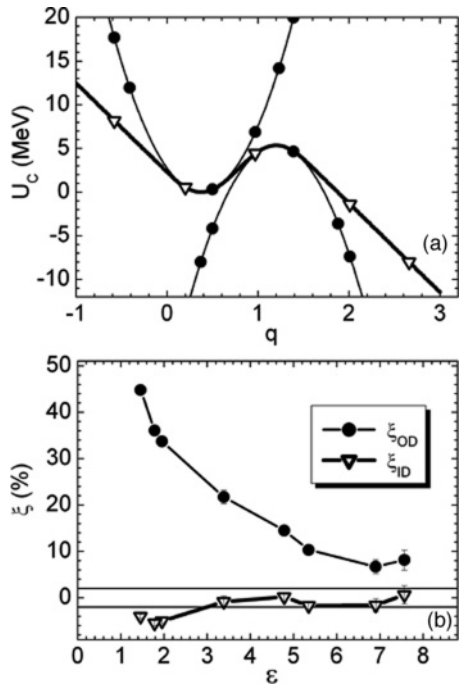

FIG. 5. Same as Fig. 3 but for the *C* potential.

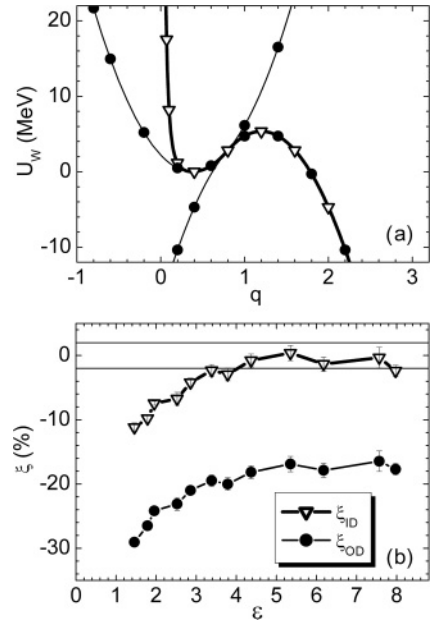

FIG. 6. Same as Figs. 3 and 5 but for the *W* potential.

larger than 3.5 does R_I agree with R_D to within 2%, exactly as happens in the case of the *H* potential.

C. The two-quadratic-parabolas potential with identical stiffnesses plus a wall (*W* potential)

Of course, the distance between the mass centers of the nascent fragments cannot be negative. This is also true for chemical applications (dissociation or association) where the distance between the ions or molecules must be positive. The potential that accounts for this requirement and keeps the advantages of the *H* one, namely the *W* potential, is again constructed of the two smoothly matched quadratic parabolas but is supplemented by an exponential wall preventing Brownian particles from coming into the unphysical region $q < 0$,

$$U_W(q) = \begin{cases} \frac{C_{qs}}{2}(q-q_{qs})^2 + \exp[100(q_{qs}-q)^3] - 1, & q < q_{qs}, \\ \frac{C_{qs}}{2}(q-q_{qs})^2, & q_{qs} \leqslant q < q_m, \\ -\frac{C_{sd}}{2}(q-q_{sd})^2 + B_f, & q \geqslant q_m. \end{cases} \quad (10)$$

The *W* potential is illustrated by Fig. 6(a). The quadratic parabolas on which it is based are also shown here as in Figs. 3(a) and 5(a) ($C_{qs} = C_{sd} = 31.44$ MeV). The resulting values of ξ_{OD} and ξ_{ID} are presented in Fig. 6(b); both are negative for all values of the parameter ε. This means that the dynamical rate is larger than the analytical ones. Moreover, ξ_{OD} lies below ξ_{ID} by about 17%. Consequently, the integral Kramers rate R_I is significantly larger than R_O. The latter does not agree with R_D at any studied values of ε [recall that $\varepsilon \gg 1$ is the prerequisite for Eqs. (3) and (4) to be valid]. However, R_I reaches the accepted agreement with the dynamical rate for large values of ε, as expected.

The low values of R_O are explained by the larger number of states contained in the upright quadratic parabola, similar to the way it was done in Sec. IV B. The value of ε at which ξ_{ID} agrees with zero within 2% is again the same as in two previous cases.

Of all the discussed potentials, the *W* potential is the closest to the realistic case (e.g., to the finite range model). Thus there is no doubt that R_O should not be used in dissipative statistical models like [8] unless one accepts about a 20% inaccuracy in the fission rate.

D. The fifth-order polynomial potential (*P* potential)

All the potentials considered previously are piece-continuous potentials. Therefore, the corresponding forces entering Eq. (1) possess the kinks. One may suspect the kink to be the cause of the inaccuracy of Eq. (4). Therefore, in this subsection we study one more case corresponding to the fifth-order polynomial potential (*P* potential), which is used in Refs. [23,29,37,38]. It reads

$$U_P(q) = Q_1 \sum_{i=1}^{5} d_i \frac{q^i}{i} + Q_2. \quad (11)$$

Here

$$d_1 = q_0 q_1 q_2 q_3,$$
$$d_2 = -q_0 q_1 q_2 - q_0 q_2 q_3 - q_0 q_1 q_3 - q_1 q_2 q_3,$$
$$d_3 = q_0 q_1 + q_0 q_2 + q_0 q_3 + q_1 q_2 + q_1 q_3 + + q_3 q_2,$$
$$d_4 = -q_0 - q_1 - q_2 - q_3,$$
$$d_5 = 1.$$

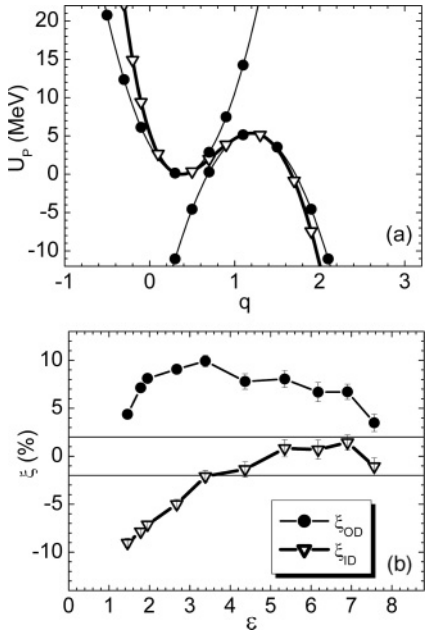

FIG. 7. Same as Figs. 3, 5, and 6 but for the *P* potential.

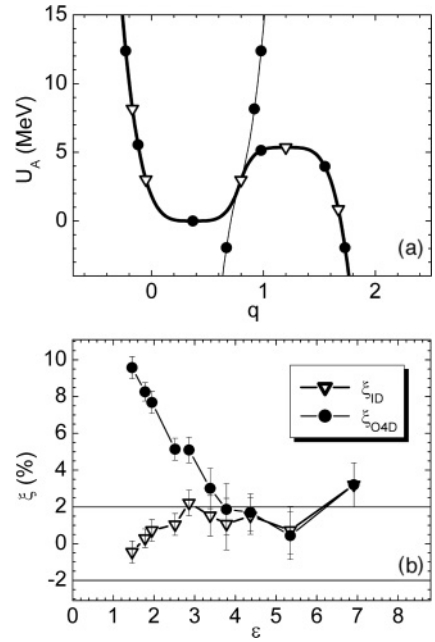

FIG. 8. Same as Figs. 3 and 5–7 but for the *A* potential. The ξ_{O4D} is calculated using Eq. (13).

The values of the parameters are $q_0 = q_{qs} = 0.375$, $q_1 = q_{sd} = 1.2$, $q_2 = 6$, $q_3 = 7$, $Q_1 = -1.7635$ MeV, and $Q_2 = 5.397$ MeV, which results in $B_f = 5.35$ MeV. The stiffnesses of the quadratic parabolas approximating the *P* potential near the quasistationary and saddle points are somewhat different: $C_{qs} = 54.22$ MeV, $C_{sd} = 40.50$ MeV. The *P* potential and the corresponding quadratic parabolas are presented in Fig. 7(a), whereas the resulting fractional differences ξ_{OD} and ξ_{ID} are displayed in Fig. 7(b) (Fig. 7 is completely analogous to 3, 5, and 6, and the notations are the same).

Ironically, R_O agrees better with R_D at higher temperatures (low values of ε), where it should not do so. No values of ξ_{OD} within 2% are reached in our calculations. Yet ξ_{ID} enters the 2% stripe at the same value of $\varepsilon \approx 3.5 - 4.0$ as in the three previous cases. The qualitative explanation of the relation between ξ_{ID} and ξ_{OD} is as follows.

In Fig. 7(a), the left branch of the approximating upright quadratic parabola is flatter than the *P* potential itself. In this sense, the situation resembles the case of the *W* potential. Thus ξ_{OD} is expected to be lower than ξ_{ID}. However, the right branch of the upright parabola in Fig. 7(a) is steeper than the potential. This corresponds rather to the situation with the *C* potential resulting in the opposite layout of the relative differences. Intuitively, one expects that the "way" from the quasistationary state to the saddle point is more important than the random walks of the Brownian particle to the left of q_{qs} and to the right of q_{sd}. Finally, $\xi_{OD} > \xi_{ID}$ in Fig. 7(b) seems to be understood as it is in Fig. 5(b).

E. The quartic-parabolas potential (*A* potential)

It is interesting to check the agreement between R_I and R_D for the potential with zero second derivatives near the quasistationary and the saddle states when Eqs. (4) and (8) are not applicable. Therefore, we perform calculations with the potential that reads

$$U_A(q) = \begin{cases} \dfrac{k_{qs}}{4}(q - q_{qs})^4, & q < q_m, \\ -\dfrac{k_{sd}}{4}(q - q_{sd})^4 + B_f, & q > q_m, \end{cases} \tag{12}$$

which is the anharmonic *A* potential. It is shown in Fig. 8(a) by the thick line, whereas the thin lines represent its components. This figure corresponds with $k_{qs} = k_{sd} = 370$ MeV.

The structure of the *A*-potential formula is very similar to that of the *H* potential. Thus it is expected that the formula analogous to Eq. (4) might be obtained from Eq. (3) in the same way. The expansion of $U(q)$ should be performed up to the fourth-order terms in this case. Finally, we have

$$R_{O4} = \frac{2(k_{qs}k_{sd})^{1/4}}{\eta\,\Gamma^2(1/4)}\sqrt{T}\exp\left(-\frac{B_f}{T}\right), \tag{13}$$

where $\Gamma(1/4) = 3.62561$ is the gamma function.

The resulting fractional differences ξ_{O4D} and ξ_{ID} are shown in Fig. 7(b). The ξ_{O4D} falls into the 2% interval near zero for $\varepsilon > 4$, whereas ξ_{ID} surprisingly enters this interval within the accuracy for all investigated values of ε. At the moment we are not able to explain why R_I agrees with R_D for $\varepsilon \approx 1$. However, we understand the relative position of ξ_{ID} and ξ_{O4D} in the same way as we do in the case of the *H* potential.

F. The two-quadratic-parabolas potential with different stiffnesses (*HΩ* potential)

The *P* potential possesses a property that the *H*, *C*, and *W* potentials do not have. Namely, its stiffnesses at the quasistationary state and at the saddle point are different. It is natural to expect that a realistic potential calculated using the liquid drop model or the finite-range model possesses different stiffnesses as well. For instance, in the work [34],

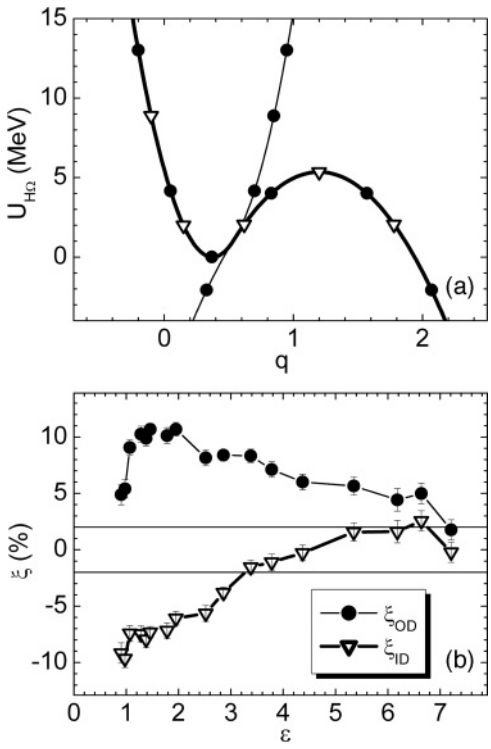

FIG. 9. Same as Figs. 3 and 5–7 but for the $H\Omega$ potential with different stiffnesses of quadratic parabolas near quasistationary and saddle states: $C_{qs}/C_{sd} = 4$.

the stiffnesses of the potential differ by a factor of 2. For this reason, we present in this section results of the calculations for the two-quadratic-parabolas potential having different stiffnesses ($\Omega = C_{qs}/C_{sd} = 4$, $C_{sd} = 19.65$ MeV). This potential (the $H\Omega$ potential) is shown in Fig. 9(a). In Fig. 9(b), the resulting fractional differences ξ_{OD} and ξ_{ID} are presented.

From this figure, one can see that R_I agrees with R_D significantly better than R_O does. The ξ_{ID} gets into the 2% interval near zero starting from $\varepsilon \approx 3.5$ as it does for most of the potentials discussed earlier. This supports our presumption that an acceptable agreement of R_O with R_D for the two-quadratic-parabolas potential with equal stiffnesses (Sec. IV A) is pure random. It is the only case of all the investigated potentials in which R_O is closer to the dynamical rate than R_I. If $C_{qs} \neq C_{sd}$, this agreement is destroyed.

For all the potentials considered, the ξ_{ID} becomes negative at low values of ε. This can be explained in the following way. Equation (3) implies equilibrium distribution of the Brownian particles inside the potential well, $\rho_{\rm eq} \sim \exp(-U/T)$. In fact, the distribution differs from the equilibrium one due to the probability current over the barrier [see, e.g., Fig. 7(b) of Ref. [21]]. The real (i.e., dynamically modeled) probability density ρ_D is very close to $\rho_{\rm eq}$ in the vicinity of the potential minimum, but it lies below $\rho_{\rm eq}$ near the fission barrier. The smaller the value of the parameter ε, the larger is the difference $\rho_{\rm eq} - \rho_D$. That is why Eq. (3) underestimates the fission rate in comparison to the dynamical calculation ($R_I < R_D$).

V. CONCLUSIONS

The problem of the accuracy of the Kramers formulas for the fission rate of heated nuclei was not often addressed in the past. In several calculations, a difference of up to 20% was revealed but the reasons were not identified [21]. Now we have made some progress, which can be summarized as follows.

The integral Kramers rate of Eq. (3), R_I, is applied to describe the fission process. Six somewhat different profiles of the fission barriers are studied. The R_I is shown to agree with the long-time limit of the dynamical rate, R_D, within 2% as the barrier height becomes about four times larger than the temperature. The amount of agreement is not affected by the barrier shape. The error within 2% is to be expected since the accuracy of the Kramers approach is of the order of $\exp(-B_f T^{-1})$.

The rate that is obtained from R_I by the use of the quadratic approximation and the infinite limits for the integrals, R_O, agrees with R_D only in the case of the two-quadratic-parabolas potential with equal stiffnesses that allows for an unphysical negative distance between the fission fragment centers. This seems to happen because of mutual cancellation of the errors. Curiously, this is the only potential for which a detailed study of the problem under consideration has been performed in the past (see Ref. [35]).

In the present paper for the five other potentials considered, R_O typically differs from R_D by more than 5%. In particular, $\xi_{OD} = (R_O - R_D)R_D^{-1}$ is about -20% for $B_f T^{-1} > 7$ for the W potential, which is the closest to the realistic one. This 20% is comparable to the non-Markovian, quantum, and multidimensional effects that are presently being studied in the literature.

Analyzing all the results, we are forced to conclude the following: there is no doubt that R_O should not be used in dissipative statistical models like [8] unless one accepts about a 20% uncontrolled inaccuracy in the fission rate. An expression similar to R_I should be used instead.

ACKNOWLEDGMENTS

M.C. is grateful to the Dmitry Zimin Foundation "Dynasty" for financial support.

[1] N. Bohr and G. A. Wheeler, Phys. Rev. **56**, 426 (1939).
[2] H. A. Kramers, Physica **7**, 284 (1940).
[3] B. Jurado, K.-H. Schmidt, and J. Benlliure, Phys. Lett. B **553**, 186 (2003).
[4] B. Jurado, C. Schmitt, K.-H. Schmidt, J. Benlliure, T. Enqvist, A. R. Junghans, A. Kelić, and F. Rejmund, Phys. Rev. Lett. **93**, 072501 (2004).
[5] K. Siwek-Wilczynska, I. Skwira, and J. Wilczynski, Phys. Rev. C **72**, 034605 (2005).
[6] C. Schmitt, P. N. Nadtochy, A. Heinz, B. Jurado, A. Kelić, and K.-H. Schmidt, Phys. Rev. Lett. **99**, 042701 (2007).
[7] S. G. McCalla and J. P. Lestone, Phys. Rev. Lett. **101**, 032702 (2008).
[8] J. P. Lestone and S. G. McCalla, Phys. Rev. C **79**, 044611 (2009).

[9] P. Fröbrich and I. I. Gontchar, Phys. Rep. **292**, 131 (1998).
[10] P. N. Nadtochy, G. D. Adeev, and A. V. Karpov, Phys. Rev. C **65**, 064615 (2002).
[11] L. Donadille *et al.*, Nucl. Phys. A **656**, 259 (1999).
[12] K. Pomorski *et al.*, Nucl. Phys. A **679**, 25 (2000).
[13] G. Chaudhuri and S. Pal, Phys. Rev. C **65**, 054612 (2002).
[14] A. V. Karpov, P. N. Nadtochy, E. G. Ryabov, and G. D. Adeev, J. Phys. G **29**, 2365 (2003).
[15] E. G. Ryabov, A. V. Karpov, and G. D. Adeev, Nucl. Phys. A **765**, 39 (2006).
[16] M. H. Èslamizadeh *et al.*, Moscow Univ. Phys. Bull. **63**, 24 (2008).
[17] W. Ye, H. W. Yang, and F. Wu, Phys. Rev. C **77**, 011302(R) (2008).
[18] E. G. Ryabov, A. V. Karpov, P. N. Nadtochy, and G. D. Adeev, Phys. Rev. C **78**, 044614 (2008).
[19] W. Ye, Phys. Rev. C **79**, 031601(R) (2009).
[20] Wu Feng and Ye Wei, Chin. Phys. C **34**, 551 (2010).
[21] I. I. Gontchar, P. Fröbrich, and N. I. Pischasov, Phys. Rev. C **47**, 2228 (1993).
[22] P. Fröbrich and A. Ecker, Eur. Phys. J. **3**, 245 (1998).
[23] J.-D. Bao and Y. Jia, Phys. Rev. C **69**, 027602 (2004).
[24] P. Fröbrich and G.-R. Tillack, Nucl. Phys. A **540**, 353 (1992).
[25] B. Yilmaz, S. Ayik, Y. Abe, and D. Boilley, Phys. Rev. E **77**, 011121 (2008).
[26] A. E. Gegechkori, Yu. A. Anischenko, P. N. Nadtochy, and G. D. Adeev, Phys. At. Nucl. **71**, 2007 (2008).
[27] P. N. Nadtochy, A. Kelić, and K.-H. Schmidt, Phys. Rev. C **75**, 064614 (2007).
[28] H. Hofmann and F. A. Ivanyuk, Phys. Rev. Lett. **90**, 132701 (2003).
[29] H. Hofmann and A. G. Magner, Phys. Rev. C **68**, 014606 (2003).
[30] W. Ye, Phys. Rev. C **81**, 011603(R) (2010).
[31] I. I. Gontchar, L. A. Lintnevsky, and P. Fröbrich, Comput. Phys. Commun. **107**, 223 (1997).
[32] H. Hofmann and J. R. Nix, Phys. Lett. B **122**, 117 (1983).
[33] D. Boilley and Y. Lallouet, J. Stat. Phys. **125**, 477 (2006).
[34] Y. Abe, C. Gregoire, and H. Delagrange, J. Phys. Colloq. **47**, 329 (1986).
[35] I. I. Gonchar and G. I. Kosenko, Sov. J. Nucl. Phys. **53**, 86 (1991).
[36] O. Edholm and O. Leimar, Physica A **98**, 313 (1979).
[37] I. I. Gontchar and P. Fröbrich, Nucl. Phys. A **575**, 283 (1994).
[38] I. I. Gontchar and N. E. Aktaev, Phys. Rev. C **80**, 044601 (2009).